RESEARCH ARTICLE

Over-the-Air Phase Calibration Methods for 5G mmW Antenna Array Transceivers

MARKKU JOKINEN, (Graduate Student Member, IEEE), **OLLI KURSU**,
NUUTTI TERVO, (Member, IEEE), **AARNO PÄRSSINEN**, (Senior Member, IEEE),
AND MARKO E. LEINONEN, (Member, IEEE)
Centre for Wireless Communications, University of Oulu, 90570 Oulu, Finland

Corresponding author: Markku Jokinen (markku.jokinen@oulu.fi)

ABSTRACT Calibration is essential to optimize the performance of any radio transceiver during its development and manufacturing processes. This paper proposes over-the-air (OTA) calibration methods based on measuring and calibrating the phases of phased array transceiver paths. The phase responses of each signal path with all phase shifter states were characterized using an OTA radio link in the transmission and reception modes. Scattering parameter measurements give amplitude and phase responses over the frequency range, which can be converted to the delay domain with the Fourier transform. In this paper, two new delay domain phase calibration methods are presented and compared with a previously presented frequency domain method. The best performance was achieved with the relative phase calibration method in the delay domain which uses all measurement data to find the calibration values. The other two methods, i.e., the absolute phase calibration method in the delay domain and in the frequency domain, use the average phase as the calibration value. OTA radiation pattern measurements from two prototype 5G millimeter wave transceivers were used to compare the RF performances of the calibration methods, and measurements were performed with a 100 MHz 5G new radio waveform. The radiation patterns were analyzed based on direction accuracy, power level, and side lobe level, to give a few examples. The transceiver units were calibrated using the three studied methods, and while having significantly different uncalibrated performances, after calibration, both transceivers were tuned to similar performance levels.

INDEX TERMS 5G, beamforming, calibration, millimeter-wave, phase shifter, phased array, transceiver, wideband.

I. INTRODUCTION

Fifth generation (5G) communications on the frequency range 2 (FR2) [1] and forthcoming sixth generation (6G) communication systems [2] utilize active antenna arrays to increase the effective isotropic radiated power (EIRP) of the transmitter (TX), enhance the noise figure of the receiver (RX), and separate or at least sectorize users to different directive beams. It is necessary to utilize high carrier frequencies to obtain more bandwidth for the communication to achieve the extreme data rates up to 1 Tbps envisioned by the 6G [2]. Antenna arrays are specifically important when using high operating frequencies, such as mmW [3] or sub-Terahertz (sub-THz), to compensate for the reduction of gain caused by the smaller aperture of a single antenna element [4]. With the larger effective aperture of the antenna array, the gain is increased and achievable link range is expanded without using high transmission power, which is also difficult to achieve with high-frequency devices.

A. WHY SHOULD WE CALIBRATE?
Individual antenna elements and their driving RF circuits have inherent phase and amplitude response variations due

The associate editor coordinating the review of this manuscript and approving it for publication was Feng Lin.

to manufacturing tolerances [5]. Hence, calibration can help obtain the best possible performance of the antenna array system. Some studies have suggested that calibration is not mandatory, e.g., in [6] and [7] to achieve the required performance. However, this requires that the radio frequency (RF) unit and the antenna solution are tightly integrated with small manufacturing tolerances. Even in highly integrated solutions, usually, several integrated radio modules are used to construct large arrays. Another argument against calibration is the averaging effect, which evens out the possible amplitude and phase variation in different antenna paths when the number of antennas increases [8]. However, averaging does not guarantee the best possible performance since it assumes uncorrelated errors between signal paths. In most cases, averaging stabilizes the radio performance, but calibration also improves the worse-performing radios to achieve the required performance.

The 5G specification [1] defines tolerances for the transmitted radiated power in a specified beam direction claimed by the manufacturer. The phase and amplitude calibration of the antenna array is a viable option to guarantee that the tolerances are met over a large number of devices. In addition, maximization of the output power by the calibration is one key system-level performance optimization parameter. It has a direct impact on cell coverage and to the cost of the network. A radio unit supporting a wide range of operating frequencies requires calibration for every supported frequency band. In phase-controlled arrays, the frequency difference between the calibration frequency and the signal frequency causes beam squint [9], which changes in the steering direction as a function of frequency. Phase uncertainty of the phase shifters needs to be taken into consideration in the calibration process. For example, with vector sum phase shifters it is easier to implement higher resolution than with switchable phase shifters, but vector sum phase shifters require separate calibration procedures for the best possible operation [10].

B. STATE-OF-THE-ART PHASE CALIBRATION METHODS

Successful calibration requires characterization measurements of the amplitude and phase of individual TX or RX paths, together with the connected antenna elements. The phase can be measured by changing phase and observing the amplitude changes of combined signal from the array [11] or by measuring scattering parameters (S-parameters) between the antenna array and a measurement antenna [12] by exciting all elements with a designed excitation matrix. Code modulation of phase shifter input was used to resolve the phase and amplitude of the array by using a built-in self-test (BIST) in [13]. The same method was used for OTA measurements in [14].

OTA measurements are preferred to be performed in the far-field, but also near-field measurements can be used for the phase array calibration, as well [15]. The near-field method is commonly used in phased antenna array radars [16] since their far-field distances are large compared to available

laboratory dimensions. Near-field measurement requires precise movement of the measurement probe and the same probe movement raster as the antenna raster, to keep channel response constant for all antenna elements. Measurements can also be performed in midfield [17], where measurement distance is in the near-field of the antenna array but in the far-field of the individual antenna element. The mid-field measurement requires precise movement of the measurement antenna and calculating the compensation factor compared to the far-field case.

One simple and efficient way to measure an antenna array in far-field is to measure every antenna individually [18]. However, this requires that antenna elements are activated and deactivated one at a time, or otherwise separated in time, frequency, or code domains. Antenna separation by different spreading codes is impossible with the phased array if it has only one shared digital signal path. Transmit-reception switches are used in time-division duplex (TDD) systems to connect reception and transmission paths to a shared antenna element [19]. The 5G mmW prototype unit [20] used as the measurement platform in this paper is implemented with TDD switches. TDD switches can be used to activate individual antenna paths during the calibration.

C. CONTRIBUTIONS

This paper presents an OTA method for calibrating the phase shifters used in mmW antenna array transceiver (TRX) by using an extensive set of S-parameter measurements. The previously presented frequency domain phase calibration method in [21] uses averaged phase responses of individual paths over the frequency band of interest in order to calculate the phase errors and the calibration coefficients. In this paper, we extend the phase calibration method in frequency domain to delay domain calibration method. The main benefit of using the delay domain method is the possibility to filter out the unwanted signal reflections caused by the measurement environment.

The frequency domain S-parameter results are converted to the delay domain via inverse Fourier transform (IFT). The delay domain analysis uses either the average phase information, in this paper called absolute calibration, or the full phase information over phase shifter states, in this paper called relative calibration, to calculate the calibration values. In addition to the phase errors, also amplitude variations of the individual paths are studied. The OTA measurements and calibrations are performed for two different RF units, both operated in TX and RX modes. Performances of three calibration methods are verified with OTA radiation pattern measurements and analyzed by using several performance indicators, like mainlobe and null position and sidelobe level to mention few. The performance indicators are also compared with theoretical values.

The paper is organized as follows. Section II describes the principles of antenna array calibration. Section III introduces the used prototype RF unit and the calibration measurement
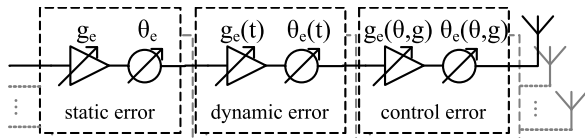
FIGURE 1. Simplified illustration of different types of errors in antenna array paths.

setup. Measurement results are then analyzed in Section IV to extract phase information with two methods. In Section V, the phase information is used to create absolute and relative phase calibration and amplitude variations are studied. Radiation patterns are measured and analyzed in Section VI to verify the effectiveness of the calibration. Finally, Section VII summarizes the work.

II. ANTENNA ARRAY CALIBRATION

Traditionally, antenna array calibration aims to minimize the deviation of amplitude and phase from the expected values. The errors can be divided into static and dynamic parts [22]. The static errors in gain g_e and phase θ_e, are not varying over time and are caused, for example, by component variations, manufacturing tolerances, and mutual coupling between antenna elements. On the other hand, dynamic errors $g_e(t)$ and $\theta_e(t)$ are time-dependent and can be caused by ambient temperature change or, e.g., component aging. The static error can be corrected with one-time calibration, which is performed during the manufacturing process. Dynamic errors require refreshing the calibrations, depending on the change rates of phase and amplitude. Either, a completely new measurement set or a reference measurement is needed. The reference measurement can be used to tune the calibration values according to the known behavior of the radio unit.

Since both phase and amplitude controls are not ideal in real implementations, there is also variation of the phase and amplitude when changing the controlled value. In Fig.1, these variations are presented with $g_e(\theta, g)$ and $\theta_e(\theta, g)$. Examples of these errors are a phase shifter which in many practical implementations changes also amplitude and amplifier biasing which also rotates the phase of the signal. Additionally, both controls usually have uncertainty in the parameter that they are controlling.

In the used 5G mmW radio unit, the phase and amplitude control are digital [23]. Hence, the accuracy limit is defined by the number of bits N_{bits} in the control word. Phase control resolution is $360°/2^{N_{bits}}$, which defines the fidelity of the calibration [15]. In OTA measurements, the physical alignment of the measurement antennas has an impact on the calibration accuracy. However, if the calibration error is smaller than the control resolution, it has only a minor effect on the calibration result.

In the antenna array, the incoming or outgoing signal phase and amplitude define the radiation characteristics of the complete array. The direction of maximum radiation can be changed by controlling the individual antenna element's phases [5]. The side lobe levels of radiation pattern can be

reduced with amplitude control [24]. Amplitude level change alone does not change the direction of the radiation. The dominant factors for creating a calibrated radiation pattern of the array are the relative phases and amplitudes between the antenna elements [16]. Due to this reason, the phase and amplitude error of the radio unit's common signal path does not affect the radiation pattern.

In this paper, we concentrate on calibrating the static and control errors. The static error over antenna paths is commonly calibrated, but also error over phase shifter states is considered in this paper. The temperature variation of the unit was only considered on the TX measurement by letting the temperature of the unit stabilize before performing the calibration measurements, since the power amplifiers (PAs) have the most significant effect on the temperature of the unit.

III. 5G MMW PROTOTYPE AND CALIBRATION MEASUREMENTS

A. MEASURED PROTOTYPE RF UNIT

In this work, a 5G mmW backhaul prototype radio unit presented in [20], [23], and [25] was used as a demonstration and measurement platform. The unit consists of two identical 16-channel 28 GHz RF beamformers that are placed on the same mechanics together with the control board. Each of the transceiver paths is connected to a 2×2 subarray. Hence, one antenna array has 16 ports that drive 64 antenna elements. The subarrays are placed in 8×2 formation [26] with a spacing of λ at 28 GHz. The unit is designed for hybrid beamforming [27], where both analog beamforming and multiple input multiple output (MIMO) can be used simultaneously [28]. In this work, we concentrate on the analog beamforming part of the unit and propose a calibration method for it. The prototype radio unit was designed to be used as backhaul radio with fixed link location, hence steering capability was designed to ease up the installation of the system, not to support user mobility. For this reason, design choices were made to obtain rather more gain with a narrower beam, but the same time limit range of steering angles. Controllable sub arrays are λ spaced generating grating lobes, which become visible with steering angles greater than $\pm 10°$ at observation angles used in this work.

A simplified block diagram of a single RF beamformer board is presented in Fig. 2. It can control the phases of the 16 transceiver paths individually by passive 5-bit phase shifters (32 phase states) with 11.25° steps. The same phase shifters are shared by the TX and RX paths. Phase shifters are not ideal, and hence their phase and amplitude error depend on the control word and operating frequency. The gains of the array halves are tuned with 5-bit controllable attenuators over 31 dB range in order to perform automatic gain control (AGC). Individual paths do not have independent amplitude control. Nevertheless, in TX mode, the amplitude of individual antenna ports can be controlled by varying the PA gate bias. However, varying the PA operation point has an impact on the phase response of the antenna path [29].

PIN diode switches are used to separate TX and RX paths in TDD mode. The switches can also be configured to disable and enable individual paths for calibration measurements as proposed in [19] and [21]. The TX paths are equipped with gallium nitride (GaN) PAs, whereas the RX paths have gallium arsenide (GaAs) low noise amplifiers (LNAs). Thus, separate measurements and compensations are needed for TX and RX paths to achieve reciprocal behavior that is crucial for TDD systems. A GaAs subharmonic mixer converts a 4 GHz intermediate frequency (IF) to the 28 GHz RF.
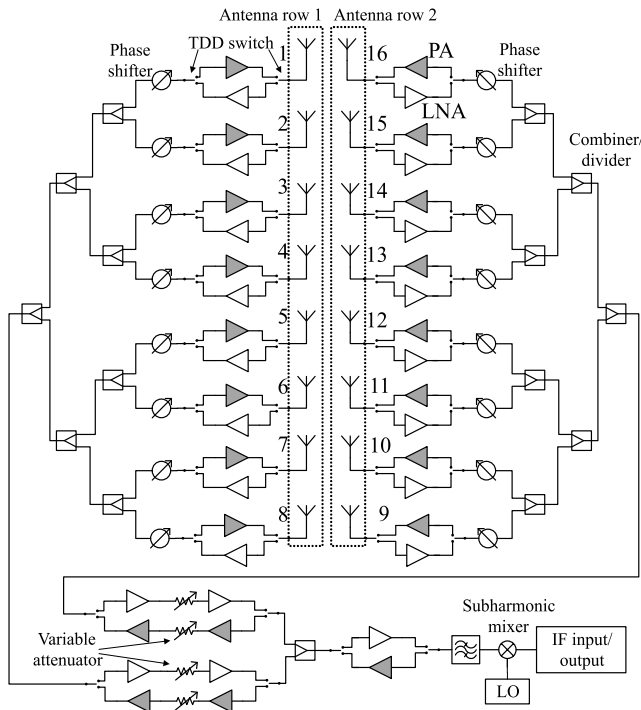
FIGURE 2. Architecture of 5G mmW prototype RF beamformer board from [21].

In this design, discrete RF components are mounted on a printed circuit board (PCB). The antenna array is implemented on another PCB that is attached to the RF board by using SMPM bullet connectors. Hence, the main sources of phase and amplitude error on the RF PCB are variations between the components, wire bonding, and component assembly. Also, the individual antenna elements and the attachment of the antenna array PCB to the RF transceiver PCB may cause significant amplitude, and in particular, phase error. For example, antenna matching [30] has a direct impact on the PA operation, that in turn has a direct impact on the overall phase and amplitude of the specific RF path.

The analog beamforming weights, i.e., the phase shifter values of each RF path are calculated using the discrete Fourier transform (DFT) method [31]. The method creates a progressive phase excitation to the antenna ports [32]. For storing phase calibration and PA biasing values Microchip 24AA025E48 2 kbit EEPROM chip was used.

B. OTA CALIBRATION MEASUREMENT SETUP

In 5G, the overall RF performance is characterized by using OTA measurements [1]. Moreover, as the OTA responses include all the errors of the platform, the calibration measurements should also be performed OTA. As the input of the TX mode is on IF and the output is at RF (or vice versa in RX mode), the measurements must be performed over frequency conversion. Traditionally, the phase of the signal is challenging to characterize over frequency conversion, at least without using a reference signal or a reference mixer. In order to overcome this, we use the full mmW link, i.e., both TX and RX, to enable the OTA measurement of each individual TRX path. The local oscillators (LOs) of both TRX units are locked to the same frequency reference to enable static phase over a long measurement period. The overall measurements are performed from the TX IF port to the RX IF port. Hence, the OTA measurement can be done without mmW frequency support from the measurement equipment.
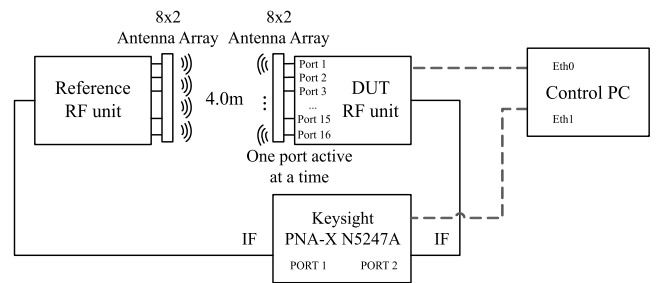

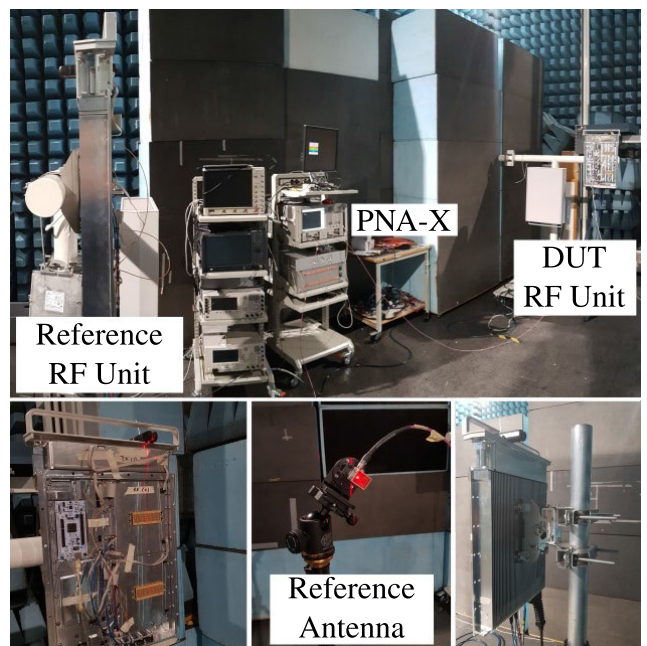**FIGURE 3.** OTA calibration measurement setup from [21].

FIGURE 4. Photographs of 5G mmW OTA measurement setup.

The block diagram of the measurement setup is presented in Fig. 3, and a photograph of the setup is shown in Fig. 4. The OTA setup was placed in an RF anechoic chamber to reduce external interferences. We used PNA-X vector network analyzer (VNA) to measure S-parameters between

the device under test (DUT) and a reference RF unit in the OTA calibration measurements. Two RF units were measured in both the RX and TX mode, other unit acting as a reference unit. The measurements were conducted to all antenna paths with all phase shifter states using the TRX switch to enable and disable paths and direct digital control to change phase shifter control words.

The calibration measurement time for the whole antenna array was approximately 10 min with 512 measurements. The calibration time is dominated by the measurement, the time for post-processing data is insignificant. If the calibration method would be used for a larger array, the measurement time would increase linearly as the number of antennas is increasing. The calibration measurements were automated by Matlab-based control software. Measurement system calibration is not needed because the phase measurement is relative, and hence the calibration is performed by normalizing with a reference antenna path. The effect of RF cabling used in the measurement setup becomes evident in the delay domain data analysis, which is discussed in Chapter IV-A.

IV. PHASE MEASUREMENT ANALYSIS

The S-parameter measurements were performed over the whole operational bandwidth of the DUT, ie. at 26.2 – 29.0 GHz RF with the fixed LO frequency of 12.0 GHz. With the sub-harmonic mixer used, this corresponds to 2.2 – 5.0 GHz IF. The measured 2.8 GHz bandwidth covers full n261 and most of the n257 bands at FR2 of the 5G standard [1]. Multiple bandwidth options are specified for FR2; options are 50, 100, 200, and 400 MHz. In this work, 100 MHz was selected as the signal bandwidth (BW) for further analysis.

A. DELAY DOMAIN IMPULSE RESPONSE ANALYSIS

Measured S-parameter data are first converted to the delay domain. The delay domain analysis is beneficial if measurements need to be done in a multi-path environment since it enables selecting only the line-of-sight path of the signal. In lab environment, multi-path components can be controlled, but more significant multi-path environments are also possible calibration locations when the delay domain filtering is used. A flow diagram of the delay domain analysis is presented in Fig. 5 (path IV-A). Inverse fast Fourier transform (IFFT) is used to convert the S-parameter data $S_{21,i,k}(f)$ to delay domain impulse responses (IR) $h_{i,k}(\tau)$, where i is the TRX path and k is the phase shifter state. The measurement parameters must be adequate to capture all required propagation delay taps after the IFFT. The maximum detectable delay is defined as

$$\tau_{\max} = \frac{1}{\Delta f} = \frac{N_{\text{points}} - 1}{\text{BW}_{\text{meas}}}, \tag{1}$$

where N_{points} is the number of frequency points, BW_{meas} is the measurement bandwidth, and Δf is the separation between adjacent frequency points. In our measurements,

$\text{BW}_{\text{meas}} = 2.8$ GHz and $N_{\text{points}} = 2801$, leading to maximum delay of $\tau_{\max} = 1$ μs which corresponds around 300 m maximum propagation distance in free space. This is more than enough to accommodate the delays of the OTA channel and the measurement setup including the electrical length of the RF cable.

The IR of a single TRX path with all 32 phase shifter states is shown in Fig. 6. The delay is further converted to propagation distance in free space in order to ease the analysis of the individual propagation paths. Note that for the sake of clarity, only amplitudes are presented. However, the measurement results contain complex-valued data, thus including the phase of each tap in the IR. We should note that the phase shift as such does not change the delay significantly and hence all measurements look very similar in amplitude. The IR data show multiple propagation paths because the signal is reflecting forth and back from the aluminum bodies of the RF units. An illustration of this is presented in Fig. 7. The position of line-of-sight (LOS) path is defined by the measurement cable's length and the OTA propagation distance. The electrical lengths of the cables were approximately 3 m at both ends of the link and the OTA distance was 4 m. This leads to around 10 m total propagation distance. In Fig. 6, the propagation distance of the LOS peak is 10.8 m. The majority of the additional electrical length originates from the RF units. The reflections, seen in Fig. 6, are separated by two times the measurement distance. The reflections are rather substantial because the RF units were aligned accurately to face each other. The amplitude of the reflected signal was significantly reduced when the alignment was changed. However, accurate alignment is essential for accurately characterizing the phase of each path.

For frequency domain data, multiple propagation paths cause fading to the phase and amplitude responses, which impact the phase measurements and, eventually, the calibration coefficients. However, proper IR analysis over a wide enough bandwidth can mitigate this effect by choosing only the desired propagation, i.e., LOS path for the phase and amplitude analysis. The propagation path with the maximum amplitude is selected for the further analysis. There is no need for the reference measurement or the VNA calibration since the data are gathered only from one delay tap. However, the method requires that the maximum amplitude delay tap should not change between the phase shifter states or active TRX paths.
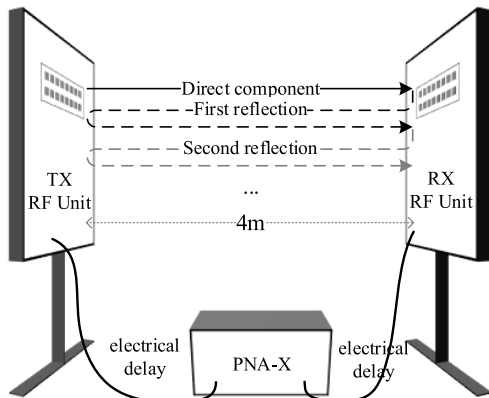
V. CALIBRATION METHODS

In this section, two different phase calibration methods are presented. In the first method, only a single calibration coefficient per TRX path is defined by using the delay domain data to minimize the phase offset of each TRX path. The delay domain data are also used to calculate the beamforming coefficients to each spatial direction based on data from all TRX paths and phase shifter values in the second method. For the TX, the amplitudes of the paths are balanced by using PA biasing before calibrations to highlight the impact of different
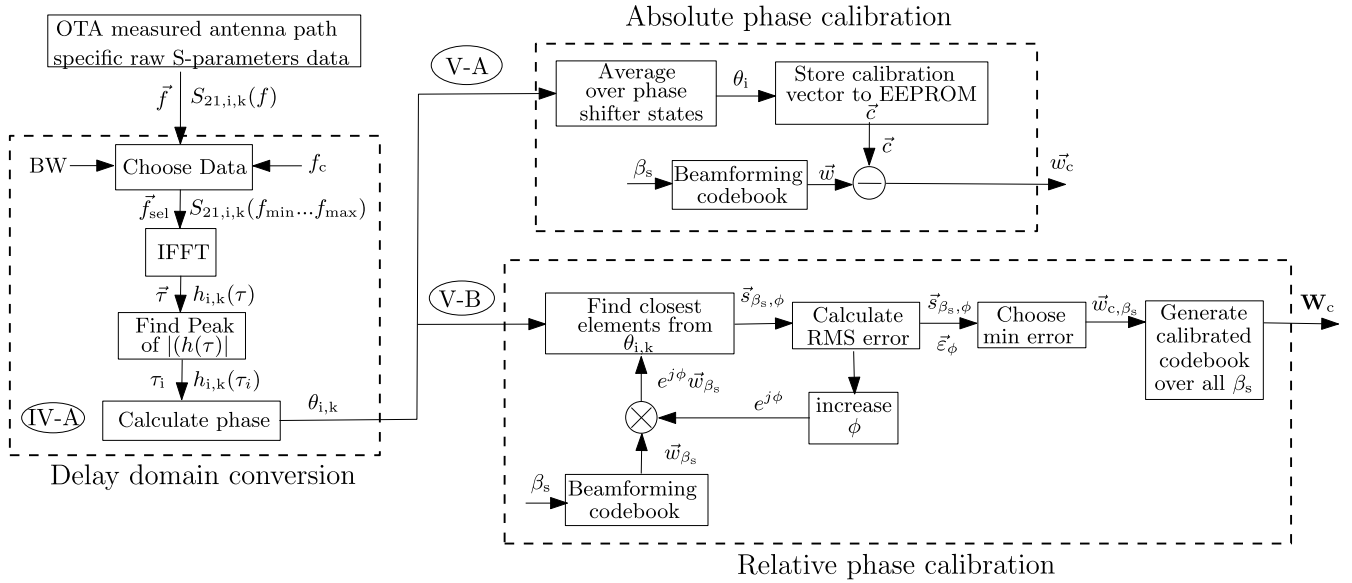
FIGURE 5. Flow diagram of the calibration processes. The delay domain analysis (path IV-A) is discussed further in Chapter IV-A, the absolute phase calibration (path V-A) in Chapter V-A and the relative phase calibration method (path V-B) in Chapter V-B.
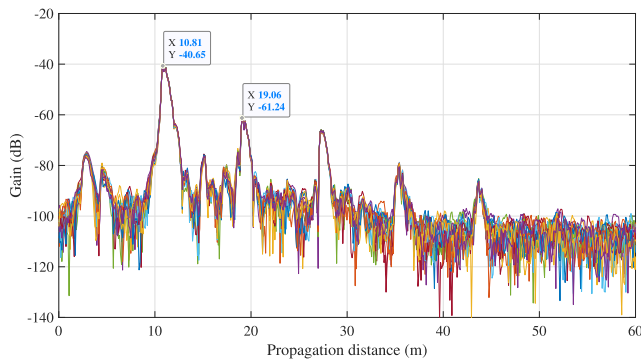
FIGURE 6. IR of a single TRX path over different phase shifter values and full measurement bandwidth. Multiple paths shown in the IR are multi-bounce reflections from the mechanics of the TRX units.

FIGURE 7. Illustration of the direct path and the multi-bounce reflections between the TRX units.

phase calibration methods. The phase calibration methods are applied for TX with and without amplitude calibration. For RX, only the phase is calibrated due to the lack of amplitude control.

**Algorithm 1** Calculate Steering Vector $\vec{w}_c$

1: Input: $\theta_{i,k} \; \forall \; i, k$
2: **for all** i **do**
3:     calculate: $\theta_i \leftarrow$ average $\theta_{i,k}$
4:     Store θ_i to EEPROM as calibration vector $\vec{c}$
5: **end for**
6: Output: $\vec{w}_c \leftarrow \vec{w} - \vec{c}$

A. ABSOLUTE PHASE CALIBRATION IN DELAY DOMAIN

The first method uses the average over all phase shifter states of each TRX path as the calibration coefficient.

A flow diagram of both phase calibration methods is presented on the right side of Fig. 5. Absolute phase calibration method in the delay domain (paths V-A) calculates only a single calibration coefficient per TRX path i. The calibration coefficients $\vec{c}$ are saved into the electrically erasable programmable read-only memory (EEPROM) of the radio unit. The calibration vector is subtracted from the original beamforming vector $\vec{w}$ of each steering angle β_s in the TRX unit. This method is also presented in Algorithm 1.

The complex-valued phase and amplitude errors of beamforming coefficient, i.e., the measured weight subtracted by the ideal weight for all TRX paths, are presented in Fig. 8. Hence, 32 data points are drawn for each of the 16 TRX paths. The averages of each radio path's data are set as the calibration coefficient. For this particular TRX array design, two 8-element antenna rows have different phase offsets. Thus, they are located on different sides of the circle. The average calibration aims to rotate the point clusters close to the zero angle. Hence, the average calibration does not compensate for all phase variations over the states, and the residual variation depends on the phase shifter itself.
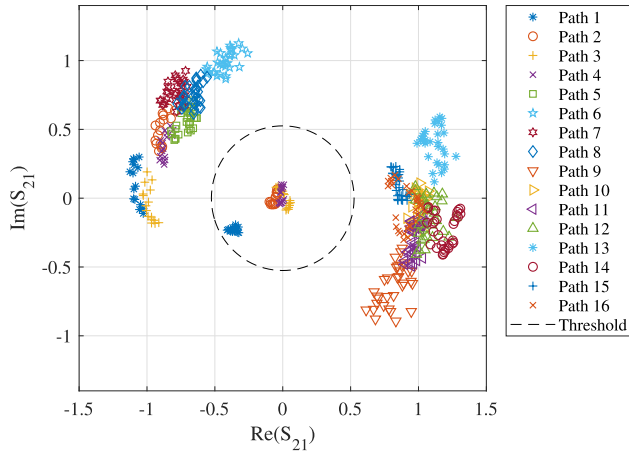
FIGURE 8. Normalized errors presented in IQ plane over different phase shifter states and TRX paths. The errors are calculated as a difference between the ideal and the measured beamformer coefficients. The deviation over different states shows the amplitude and phase error across the states whereas the location of the point centroids shows the static error of each TRX path.

Calibrating only the average would probably be sufficient for high-accuracy phase shifter implementations. However, the information of the residual variation can improve the calibration, and this technique is discussed in the following section.

B. RELATIVE PHASE CALIBRATION IN DELAY DOMAIN

The main idea of the second method, called relative phase calibration in delay domain, is that the measured variations are not treated as errors, and the entire beamforming codebook $\mathbf{W}_c$ is rebuilt based on the measurements.

This phase calibration method is using specific calibration coefficients for each beam steering angle. The entire data set $\theta_{i,k}$ measured from all TRX paths i, and phase shifter states k can be used to find the best possible combination to steer the beam in a certain spatial direction. Furthermore, instead of using a single TRX as a reference phase, the reference ϕ is chosen such that it can be different for every steering angle. The same kind of idea, where the reference was selected from phase shifter states, is presented [18]. In our method, the reference can be selected freely. Simulations for generating nulls with vector modulator phase shifter and similar calibration method was presented in [33]. A flow graph of the relative phase calibration is shown in the lower right side of Fig. 5 (path V-B). The same procedure is presented in more detail with Algorithm 2, where $\vec{w}_{\beta_s}$ is the ideal beamformer and $\vec{w}_{c,\beta_s}$ is the calibrated beamformer. $\vec{s}_{\beta_s,\phi}$ is used to store beamformer candidates calculated with different reference phase values. For each desired steering angle β_s, the ideal beamformer is rotated by small ϕ steps in the IQ unit circle. For every rotation step and steering angle, we calculate the root-mean-square (RMS) error between the ideal and measured beamforming coefficients as

$$\varepsilon_{\beta_s,\phi} = \sum_{i=1}^{N_{\text{TRX}}} |s_{\beta_s,\phi,i} - e^{j\phi} w_{\beta_s,i}|^2, \qquad (2)$$

Algorithm 2 Calculate Codebook $\mathbf{W}_c$

Require: $\theta_{i,k} \ \forall \ i, k$
1: **for all** β_s **do**
2:      **for all** ϕ **do**
3:          **for all** i **do**
4:              Find: $\hat{k} \leftarrow \underset{k \in 1,...,2^{N_{\text{bits}}}}{\arg \min} |\theta_{i,k} - e^{j\phi} w_{\beta_s,i}|$
5:              Store the best: $s_{\beta_s,\phi,i} \leftarrow \theta_{i,\hat{k}}$
6:          **end for**
7:          $\varepsilon_{\beta_s,\phi} \leftarrow$ Calculate (2)
8:      **end for**
9:      Find: $\hat{\phi} \leftarrow \underset{0 \le \phi < 2\pi, \phi \in \mathbb{R}}{\arg \min} \varepsilon_{\beta_s,\phi}$
10:      Store the best: $\vec{w}_{c,\beta_s} = \vec{s}_{\beta_s,\hat{\phi}}$
11: **end for**
Ensure: $\mathbf{W}_c = \begin{bmatrix} \vec{w}_{c,1} & \dots & \vec{w}_{c,\beta_s} & \dots & \vec{w}_{c,N_\beta} \end{bmatrix}$

---

where N_{TRX} is the number of TRX paths. The smallest error is selected and the corresponding values are used as the steering vector $\vec{w}_{c,\beta_s}$ for each particular steering angle. In the experimental setup the onboard EEPROM was not large enough for storing the calibration vector due to the fact that each steering angle requires its own set of calibration coefficients. Instead, the phase shifters are controlled individually with codebook $\mathbf{W}_c$.

Some phase shifter values were at a significantly lower amplitude than others due to the wire bonding and the die attachment manufacturing defects of the bare die phase shifter components. Those values are located close to the origin in Fig. 8. These phase shifter values were discarded in the relative phase calibration vector by setting a threshold for the amplitude shown in Fig. 8. An 8 dB threshold compared with the highest power level of the TRX path was used. All samples inside the threshold circle were discarded and the rest of the phase shifter values were used for beam steering purposes. Regardless of the screening of data, a good enough steering vector was found for demonstration purposes.

In the absolute phase calibration method, the effect of low amplitude samples is mitigated since the final phase calibration value is based on the average of the complex values and the low amplitude reduces the influence of the phase of those samples.

C. TX GAIN CALIBRATION AND IMPACT OF AMPLITUDE VARIATIONS

Especially in case of large amplitude errors, the phase only calibration may not be enough to achieve accurate beam steering. Moreover, the amplitude errors affect the phase errors, and those have a combined effect on the system. In our measurement platform, the amplitude variation was a more severe problem in the TX than in the RX. Furthermore, as the TRX path did not have path-specific amplitude control, the impact of amplitude errors was studied on the TX, only. The TX amplitude control of the antenna array was implemented by varying the bias currents of the PAs by

controlling their gate voltages [29]. However, due to the fact that the PA biasing has an impact on the phase of the signal, the bias values were set prior to the phase calibration.

Two sets of PA operation points were used in the measurements: (i) equal bias currents and (ii) equal output powers. First, equal bias currents were applied to all PAs. Maintaining the PA currents equal is usually considered as the default PA calibration that aims to operate all PAs in the same operation point. However, equal current leads to varying output powers from different TX paths in our platform.

In second scenario, bias currents were set individually for each PA, based on individual TX path OTA output power measurement over a 100 MHz channel bandwidth, so the TX powers were as close as possible to each other to achieve uniform amplitude excitation. The individual bias currents were tuned down from the equal current scenario to guarantee PA stability in non-usual operation modes. In the following sections, this method is called amplitude calibration. Note that it does not utilize all available output power of the TX array. However, it is the only way to equalize the amplitude variations over TX paths and achieve the best phase calibration performance in our measurement platform.

Normalized average gains over the phase shifter states of all TX paths from two different RF RF units are presented in Fig. 9a. Range of maximum and minimum values is presented with an error bar since the gain varies over the phase shifter control words. The maximum gain is used as reference for normalization of gains in each biasing scenarios (cases (i) and (ii)). Significantly lower gains of individual phase shifter states are omitted from Fig. 9a since those are not used in the phase calibration. A significant variation of TX path gains is observed when the PAs are biased to the equal current. Especially with RF unit 1, paths 1-8 have much higher gain than the others, that was caused by the unequal gains of the first driver stage amplifiers where the signal is divided into the halves of the array, as shown in Fig. 2. There is no apparent difference between array halves in RF unit 2, but the amplitude fluctuates between paths. As expected, the TX amplitude level stays much flatter after the adjustment of PA bias values.

The RX amplitude levels from both RF units and the results normalized to the maximum amplitude of each board are shown in Fig. 9b. There is some variation in the RX amplitude levels, but no possibility to adjust the amplitude levels of the individual RX paths in the used RF platform.

## VI. ARRAY RADIATION PATTERN MEASUREMENT RESULTS

A. PHASE ERROR DISTRIBUTION OF DIFFERENT CALIBRATION METHODS

The distance of steering vector phases from the ideal values can be extracted from the calibration measurements. All measured steering angles were analyzed with different calibration methods, and the results are shown in Fig. 10. The figure is limited to $\pm 90°$ for better readability, but
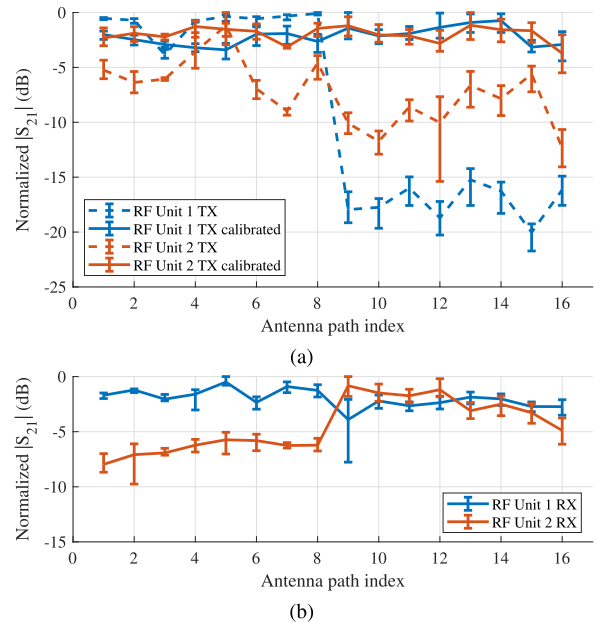
FIGURE 9. Gain variation over antenna paths on (a) TX and (b) RX, measured from IF of the DUT to IF of the reference unit over 100 MHz bandwidth. Maximum and minimum gain over phase shifter states is presented with error bar. Gains are normalized to maximum value of each measurement.

uncalibrated samples extend to full rotation on the unit circle. Since phase errors are distributed on a unit-circle, where $+180°$ and $-180°$ represent the same phase error, the error distributions can not be analyzed with standard distribution functions. Instead, circular distribution function [34] was used to create a fit to the measured data. Circular distribution can be thought as linear distribution wrapped around the unit-circle, so the phase error can not have arbitrarily large values, but values wrap around at $\pm 180°$.
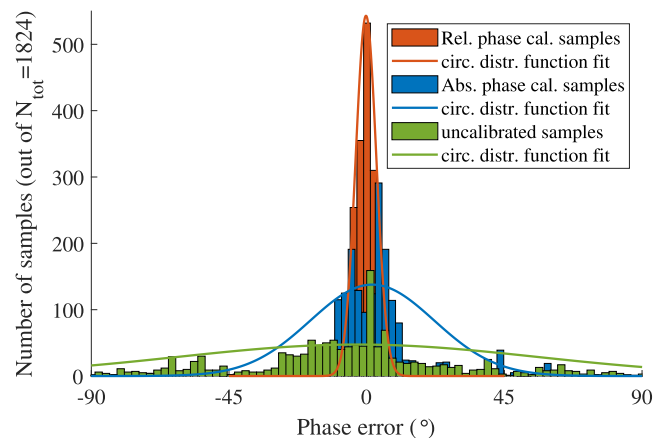
FIGURE 10. Phase error distribution over all phase shifter states used for steering the radiation pattern. Distribution fits calculated with circular distribution function which can process data on the angular values of $\pm 180°$. The figure is limited to $\pm 90°$ for better readability.

Uncalibrated samples have a visible peak at 0 error since each steering vector has one 0 error sample which is used to compare other observations. Uncalibrated samples have standard deviation of $\sigma = 58.8°$. In the absolute calibration, the reference for all steering angles is selected as

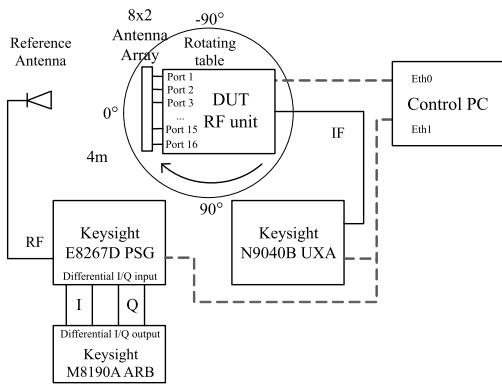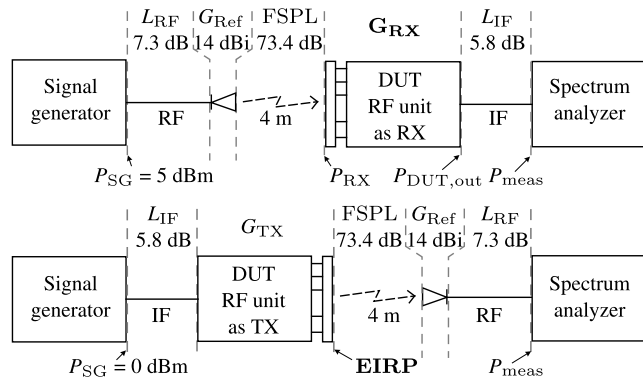**FIGURE 11.** RX radiation pattern measurement setup from [21].

FIGURE 12. Power levels and gains in different parts of the radiation pattern measurement setup.
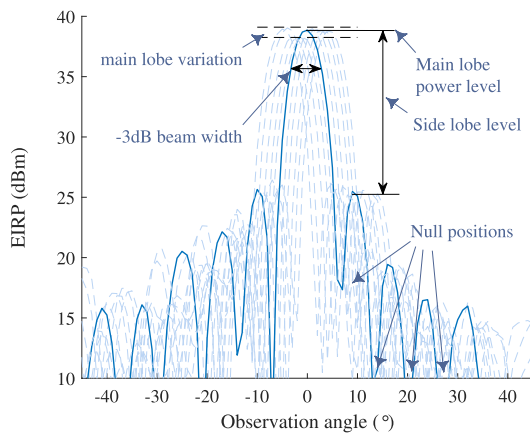

FIGURE 13. Illustration of the figures of merit used to describe the performance of the calibration methods.

FIGURE 14. Normalized RX radiation patterns measured with 5GNR signal with and without calibrations over ±45° and (b) a zoomed-in version to observe better the differences. The example steering angle is −4°.

B. MEASURING RADIATION PATTERNS

The performances of the calibration methods were validated by radiation pattern measurements with a 5GNR waveform. The measurements were performed with and without phase calibrations. Two RF units (1 & 2) were measured in RX and TX modes. The phase calibrations are applied with and without amplitude calibration in TX mode. An RF frequency of 28.0 GHz was used in the measurements, and the IF frequency was set to 4.0 GHz. The radiation patterns were measured with steering angles −10°, +10°, and from −5° to +5° with 1° steps. A phase interpolation method [7] was used to achieve higher steering angle resolution than theoretically possible for 5-bit phase shifters.

The OTA radiation pattern measurement setup is presented in Fig. 11. The RF unit is mounted on a rotating table and rotated over azimuth quarter-plane of [−45°, +45°] with 1° steps. The DUT is fixed during the calibration, and the rotating table is used only for the performance characterization. Traditionally, a continuous wave (CW) signal is used in radiation pattern measurements. We used a 100 MHz wide 5G NR 64-QAM CP-OFDM modulated

the average of phases over phase control words, this means that fewer samples are precisely at 0 error. Most of the samples are located half phase shifter resolution away from 0 error, making the shape look like bimodal distribution. Nevertheless, to compare performance with other methods, distribution was calculated with circular distribution function and a deviation of $\sigma = 20.3°$ was achieved. The phase reference is selected for each steering angle separately in the relative calibration method, and the error values are centered around the 0 error value, with the smallest standard deviation of $\sigma = 3.3°$.
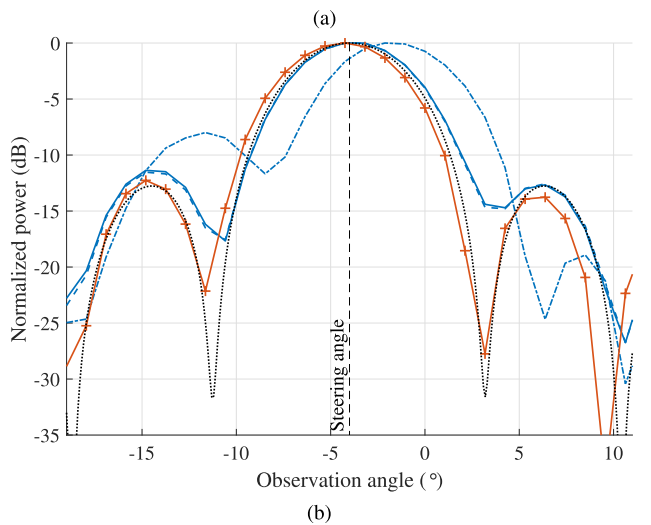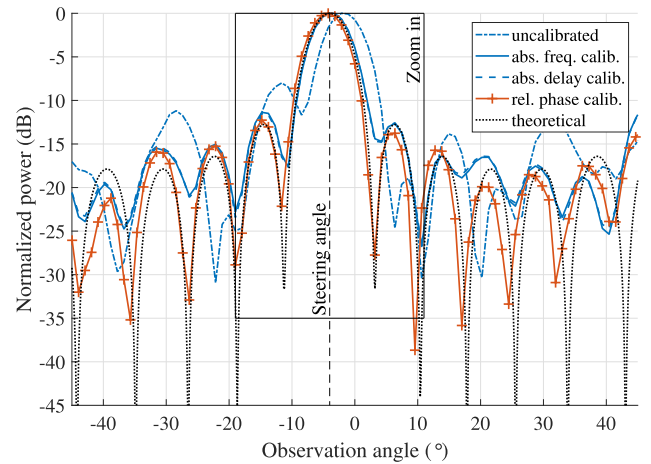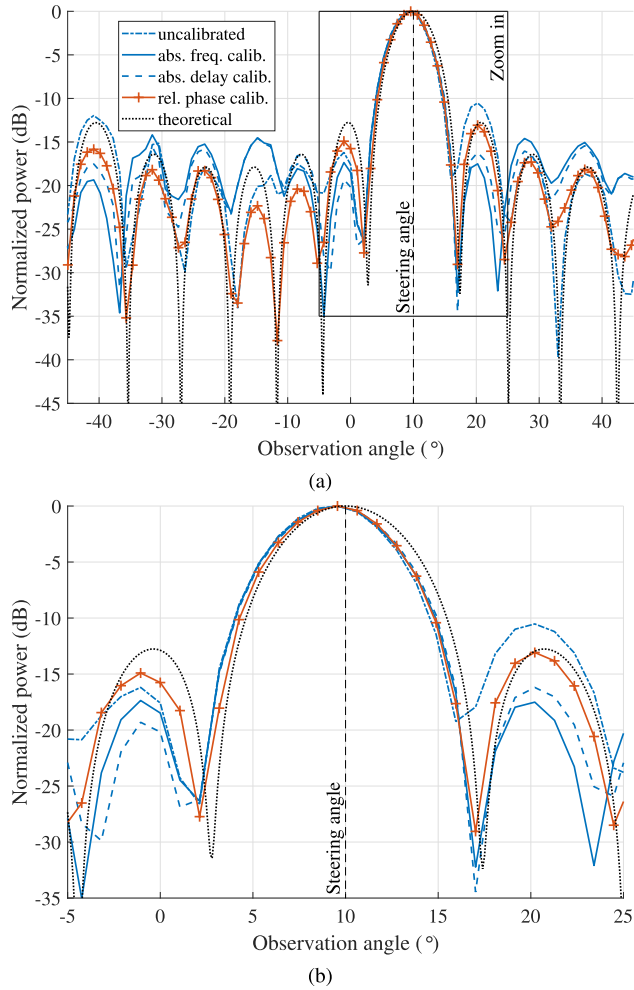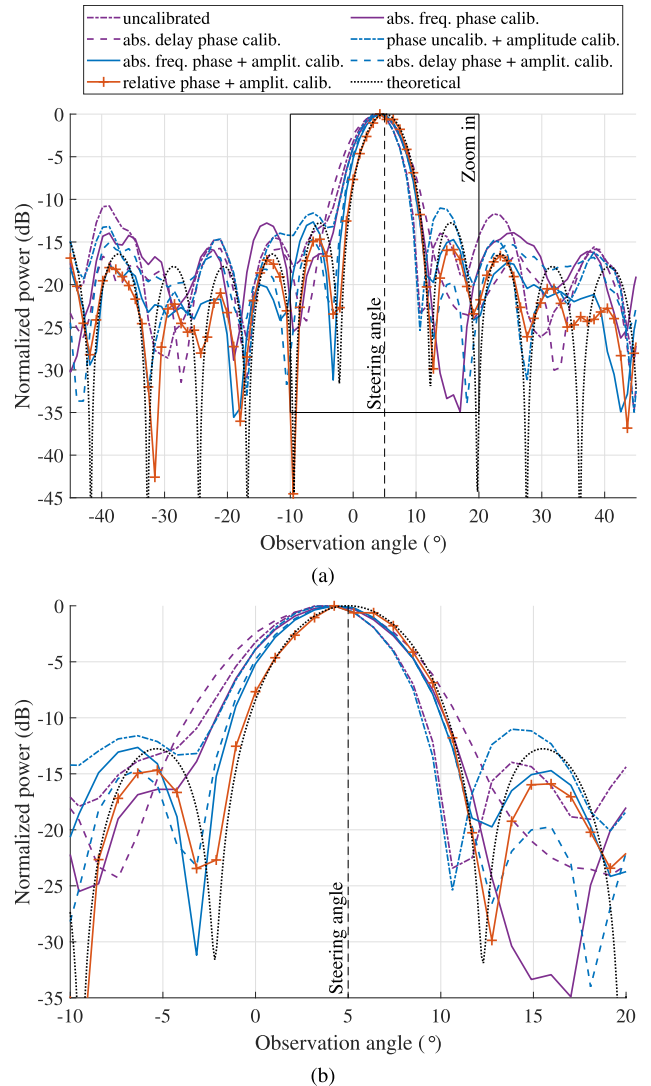
FIGURE 15. Normalized RX radiation patterns measured with 5GNR signal with and without calibrations over ±45° and (b) a zoomed-in version to observe better the differences. The example steering angle is +10°.

signal [1] to emulate a typical operation condition of the unit. The test signal was generated with an arbitrary waveform generator (ARB) and upconverted to 28 GHz with a vector signal generator (PSG) in the RX measurement. A standard gain horn antenna (A-info LB-28-15) was used as a reference antenna to radiate the test signal towards the DUT. The signal analyzer (UXA) measured the 100 MHz wide test signal at the IF frequency. The TX measurements were performed with a similar setup, but the UXA was connected to the reference antenna and received the signal at 28 GHz. The PSG and the ARB were used to feed the modulated signal to the DUT at the IF frequency. The reference antenna was placed perpendicular to the antenna array center point 4 m away from the array when the rotating table position was 0°. Line lasers were used for accurate alignment. We programmed a Matlab-based control software to automatize the radiation pattern measurements.

The signal level attenuates when the beam is steered away from the broadside direction of the antenna array. This behavior is caused by a change of patch antenna illumination when the antenna is physically rotated [24]. The antenna element radiation pattern includes a sub-array pattern [26],

FIGURE 16. Normalized TX radiation patterns measured with 5GNR signal with and without calibrations over ±45° and (b) a zoomed-in version to observe better the differences. The example steering angle is +5°.

which affects the amplitude of the radiation pattern. Antenna array offset affects radiation pattern angles by deviating the measured samples at the edge of the radiation pattern. These effects were compensated from the measurement results mathematically. Furthermore, the measurement results were compared with the theoretical ones.

The link budgets of the RX and TX OTA measurements are shown in simplified block diagrams in Fig. 12. Calculated free space path loss (FSPL) for a 4 m measurement distance, and the center frequency of 28 GHz is 73.4 dB based on [35]. The cable losses on RF and IF were L_{RF} = 7.3 dB and L_{IF} = 5.8 dB. The reference antenna gain (G_{Ref}) was 14 dBi. The reference antenna gain, the cable losses, and the free space path loss were subtracted from the measurement results. In TX mode, EIRP was used to measure the signal levels, and in RX mode, RX gain (G_{RX}) was used to compare the effect of different calibration methods on signal levels. In the TX measurements, the signal generator power
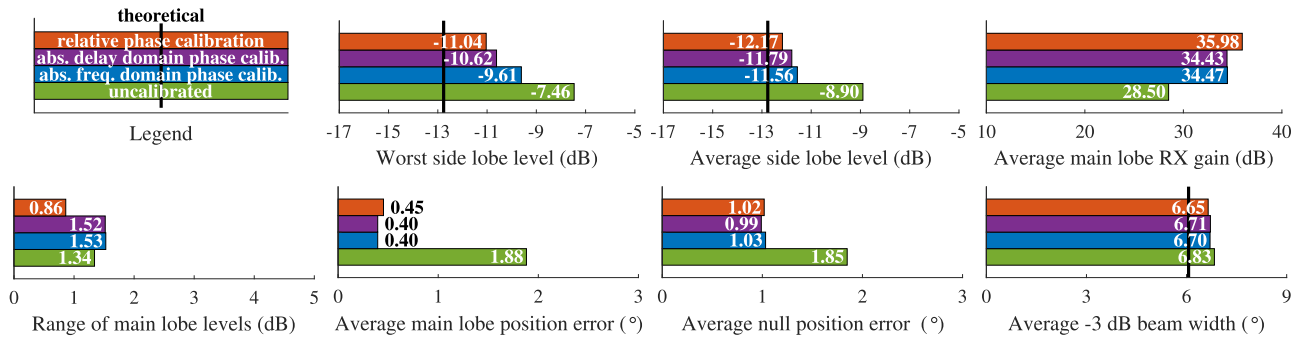
FIGURE 17. Combined calibration figures of merit of RX analyzed across all 13 different steering angles at 28GHz for RF unit 1.
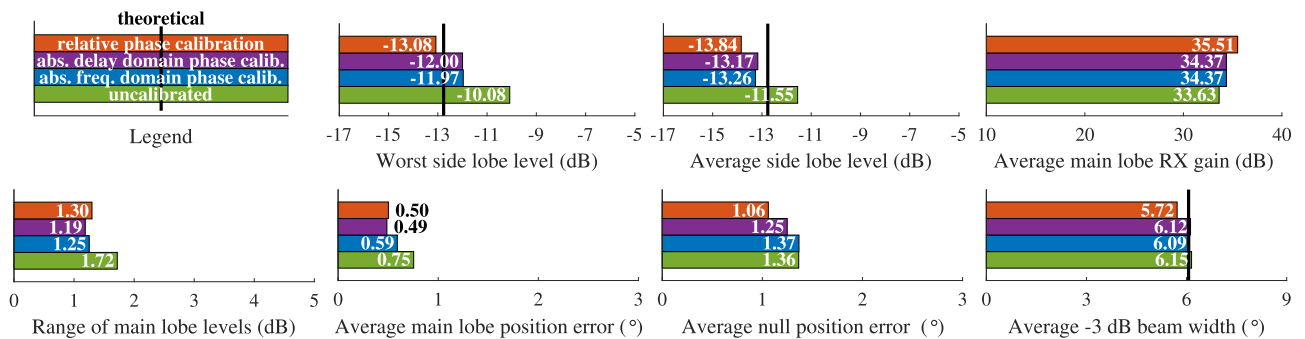

FIGURE 18. Combined calibration figures of merit of RX analyzed across all 13 different steering angles at 28GHz for RF unit 2.
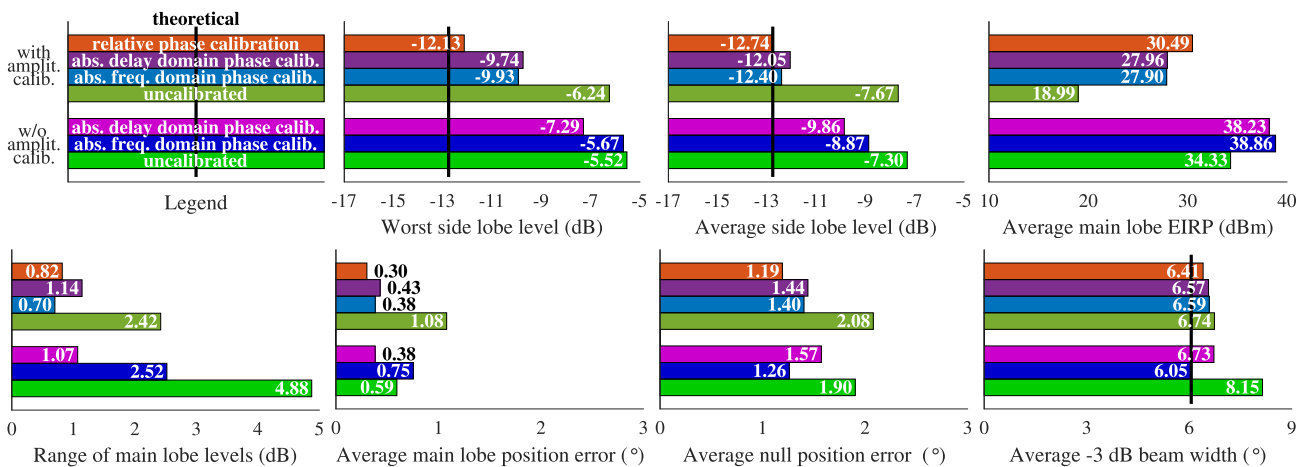

FIGURE 19. Combined calibration figures of merit of TX analyzed across all 13 different steering angles at 28GHz for RF unit 1.

$P_{SG} = 0$ dBm, and in the RX measurements $P_{SG} = 5$ dBm was used.

The key performance indicators to be analyzed based on the radiation pattern measurements are the main lobe level, side lobe level, 3 dB beamwidth, main lobe position error, and null position error. The definitions of the indicators are graphically illustrated in Fig. 13. The indicators are calculated for each steering direction and analyzed as mean and worst-case values over the steering angles. The main lobe and null position errors are calculated as the differences between the measured and the theoretical radiation pattern positions. Additionally, main lobe level variation over steering angles was recorded.

Measured examples of RX and TX radiation patterns without calibration and with three calibration methods and the theoretical pattern are presented in Figs. 14, 15 and 16. Two calibration methods were presented in Chapter V and one was presented in previous work [21]. The S-parameter based method from the previous work is called the absolute phase calibration method in the frequency domain. It resembles the delay domain method but uses a frequency domain average over the band of interest instead of FFT and delay domain peak value.

There is a visible main beam pointing offset if the RX is uncalibrated and calibrations correct the error. The amplitude calibration improves the TX radiation patterns in general,
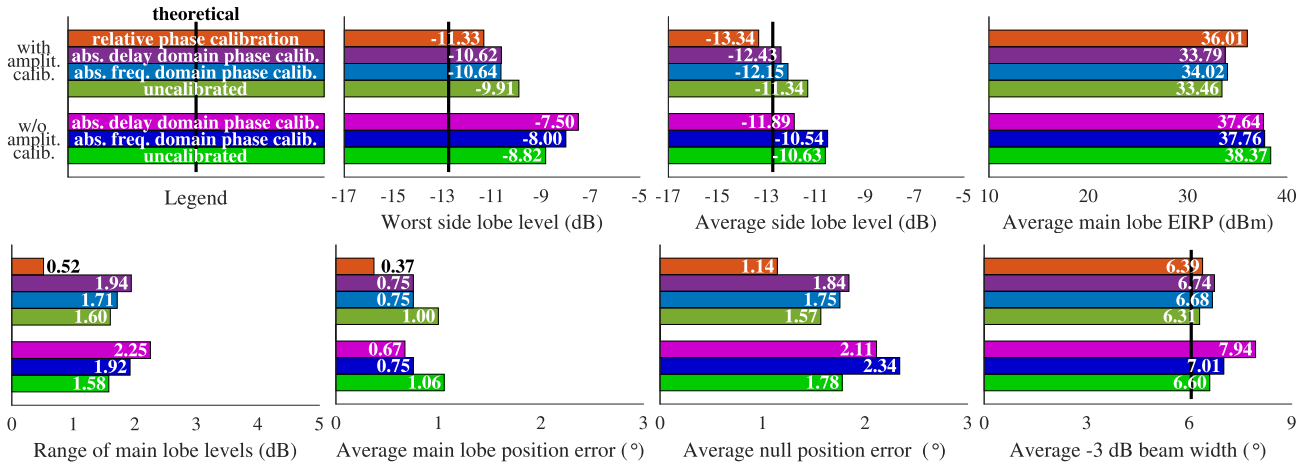
FIGURE 20. Combined calibration figures of merit of TX analyzed across all 13 different steering angles at 28GHz for RF unit 2.

and without the amplitude calibration, the beam pointing offset is noticeable. The relative phase calibration gives the consistently closest radiation pattern to the theoretical one and lowest side lobe levels. The relative phase calibration gives the best null position accuracy and depth, whereas some nulls with other calibration methods have a significant offset or high amplitude level.

C. ANALYSIS OF RESULTS

Two different RF units (1 and 2) were used for RX measurements and the results are presented in Figs. 17 and 18. Calibrations improve the average main lobe array gain and the average and the worst side lobe levels over the steering angles. The average main lobe gain increases from 0.7 to 5.9 dB when the results of the absolute phase calibration in the delay domain are compared to the uncalibrated case. Results are similar compared with the absolute phase calibration in frequency domain, which was expected because multipath components in the measurement environment were far apart. With relative phase calibration, the increase is from 1.9 to 7.5 dB. Improvement in the worst side lobe level using different calibration methods is on average of 2.0 dB, 2.5 dB, and 3.3 dB for absolute phase calibration in frequency domain, absolute phase calibration in delay domain, and relative phase calibrations in delay domain, respectively.

However, there is a significant difference between the boards, depending on how good results the uncalibrated case gives. The highest fluctuation of main lobe gain is observed if no calibration was used with the RF unit 2. The main lobe position error was calculated over measured steering angles. Naturally, it has the highest values without calibration, especially with the RF unit 1, and similar behavior is seen in the null position error in Fig. 14. The calibration does not have a significant impact on measured beamwidths. As a summary, the relative phase calibration scheme produces the best radiation pattern results. Additionally, although there is significant variation between boards without calibration, the performance of both boards can be improved and made close to equal with proper calibration.

The TX measurement results from RF unit 1 and RF unit 2 are presented in Figs. 19 and 20. In TX measurements, the amplitude calibration is performed by adjusting the PA biases as presented in section V-C. Amplitude levels were presented in Fig. 9. Amplitude calibration improved the shape of the radiation patterns, but the total power level is reduced when lowering the power output of most amplifiers. The amplitude calibration makes the phase calibration more efficient in TX mode, i.e., a more significant effect on the main lobe and side lobe levels. On average, without amplitude calibration, the main lobe level is improved by 2.0 and 1.6 dB, and the worst side lobe levels -0.3 and 0.2 dB with absolute phase calibration in frequency and delay domain, compared with the uncalibrated case, respectively. The corresponding values are 4.7 and 4.7 dB for the main lobe level and 2.2 and 2.1 dB for the side lobe levels with calibrated amplitudes. The relative phase calibration achieves the best results in TX calibrations except for some parameter combinations. Compared to the uncalibrated case, the main lobe level is improved from 0.6 to 8.9 dB with absolute phase calibration in frequency domain, from 0.3 to 9.0 dB with absolute phase calibration in delay domain, and 2.6 to 11.5 dB with relative phase calibration in delay domain when amplitude calibration is used. Average side lobe levels are improved from 0.8 to 4.7 dB with absolute phase calibration in frequency domain, from 1.1 to 4.4 dB with absolute phase calibration in delay domain, and from 2.0 to 5.1 dB with relative phase calibration.

Similarly, like on the RX side, in the TX direction there is difference between the boards without calibration. Nevertheless, with relative phase calibration in delay domain, the performance of both boards is converted to a similar level. The only exception is the EIRP which is more significantly affected by amplitude calibration on RF unit 1, since there was a larger imbalance between the antenna paths.

VII. CONCLUSION

In this paper, performances of two proposed calibration methods, absolute and relative phase calibration method in the delay domain, and previously presented absolute phase

calibration method in the frequency domain were applied to the 5G mmW phased-array transceiver. The absolute calibration method in the frequency domain uses the average phase value over the band of interest and phase shifter states as a calibration value. In the absolute phase calibration method in the delay domain, the measured frequency domain signal is first converted to the delay domain and only the LOS component is used to calculate the calibration value. The relative phase calibration method uses the same delay domain data, but instead of calculating the average over the phase shifter states, it uses the whole data set to find the best phase state combination for each steering angle.

The performances of the calibration methods were analyzed based on OTA radiation pattern measurements using a 5G NR waveform, and two RF boards in TX and RX modes. The relative phase calibration achieved the best OTA radiation pattern characteristics. The relative phase calibration improves calibration accuracy by taking advantage of variations in the phase shifter states instead of using an average phase as a correction therm. The main lobe level is improved by 11.5 dB, and the side lobe level by 5.1 dB compared to the uncalibrated radiation pattern. The average main lobe power is increased by 1.3 dB and the side lobe level is reduced by 0.6 dB in RX mode compared to the other calibration methods. In the TX mode, the main lobe power is increased on average by 2.3 dB, and the side lobe level improved by 0.8 dB.

The proposed calibration methods are based on the delay domain analysis, and this approach improves phase measurement accuracy in a multi-path environment. The validation measurements were performed in an anechoic chamber, and the delay-domain and the frequency domain methods have similar performances. The main advantage of the delay domain approach is that unwanted signal reflections from the environment or the DUT are filtered out.

REFERENCES

[1] Base Station (BS) Radio Transmission and Reception, Standard 3GPP Tech. Spec. 38.104, V18.1.0 (Release 18), Apr. 2023.

[2] A. Pärssinen. (2021). White Paper on RF Enabling 6G–Opportunities and Challenges From Technology to Spectrum. [Online]. Available: http://urn.fi/urn:isbn:9789526228419

[3] T. S. Rappaport, S. Sun, R. Mayzus, H. Zhao, Y. Azar, K. Wang, G. N. Wong, J. K. Schulz, M. Samimi, and F. Gutierrez, "Millimeter wave mobile communications for 5G cellular: It will work!" IEEE Access, vol. 1, pp. 335–349, 2013.

[4] F. Aryanfar and M. Hossain, "A quad-channel 11-bit 1-GS/s 40-mW collaborative ADC enabling digital beamforming for 5G wireless," IEEE Trans. Microw. Theory Techn., vol. 67, no. 9, pp. 3798–3820, Sep. 2019.

[5] D. Parker and D. C. Zimmermann, "Phased arrays—Part 1: Theory and architectures," IEEE Trans. Microw. Theory Techn., vol. 50, no. 3, pp. 678–687, Mar. 2002.

[6] R. Valkonen, "Compact 28-GHz phased array antenna for 5G access," in IEEE MTT-S Int. Microw. Symp. Dig., Jun. 2018, pp. 1334–1337.

[7] K. Kibaroglu, M. Sayginer, and G. M. Rebeiz, "A low-cost scalable 32-element 28-GHz phased array transceiver for 5G communication links based on a 2 × 2 beamformer flip-chip unit cell," IEEE J. Solid-State Circuits, vol. 53, no. 5, pp. 1260–1274, May 2018.

[8] K. Kibaroglu, M. Sayginer, T. Phelps, and G. M. Rebeiz, "A 64-element 28-GHz phased-array transceiver with 52-dBm EIRP and 8–12-Gb/s 5G link at 300 meters without any calibration," IEEE Trans. Microw. Theory Techn., vol. 66, no. 12, pp. 5796–5811, Dec. 2018.

[9] S. K. Garakoui, E. A. M. Klumperink, B. Nauta, and F. E. van Vliet, "Phased-array antenna beam squinting related to frequency dependency of delay circuits," in Proc. 41th Eur. Microw. Conf., Manchester, U.K., Oct. 2011, pp. 1304–1307.

[10] M. Jokinen, A. Sethi, O. Kursu, T. Rahkonen, M. E. Leinonen, and A. Pärssinen, "Iterative calibration method for integrated tunable mmW vector-sum phase shifter," in Proc. 100th ARFTG Microw. Meas. Conf. (ARFTG), Jan. 2023, pp. 1–4.

[11] S. Mano and T. Katagi, "A method for measuring amplitude and phase of each radiating element of a phased array antenna," Electron. Commun. Jpn. I, Commun., vol. 65, no. 5, pp. 58–64, 1982.

[12] R. Long, J. Ouyang, F. Yang, W. Han, and L. Zhou, "Multi-element phased array calibration method by solving linear equations," IEEE Trans. Antennas Propag., vol. 65, no. 6, pp. 2931–2939, Jun. 2017.

[13] K. Greene, V. Chauhan, and B. Floyd, "Built-in test of phased arrays using code-modulated interferometry," IEEE Trans. Microw. Theory Techn., vol. 66, no. 5, pp. 2463–2479, May 2018.

[14] Z. Hong, S. Schönherr, V. Chauhan, and B. Floyd, "Free-space phased-array characterization and calibration using code-modulated embedded test," in IEEE MTT-S Int. Microw. Symp. Dig., Jun. 2019, pp. 1225–1228.

[15] K. Hassett, "Phased array antenna calibration measurement techniques and methods," in Proc. Eur. Conf. Antennas Prop. (EUCAP)), Apr. 2016, pp. 1–4.

[16] I. Şeker, "Calibration methods for phased array radars," Proc. SPIE, vol. 8714, pp. 294–308, May 2013.

[17] H. Kong, Z. Wen, Y. Jing, and M. Yau, "Midfield over-the-air test: A new OTA RF performance test method for 5G massive MIMO devices," IEEE Trans. Microw. Theory Techn., vol. 67, no. 7, pp. 2873–2883, Jul. 2019.

[18] J. Eisenbeis, J. Pfaff, C. Karg, J. Kowalewski, Y. Li, M. Pauli, and T. Zwick, "Beam pattern optimization method for subarray-based hybrid beamforming systems," Wireless Commun. Mobile Comput., vol. 2020, pp. 1–7, Dec. 2020, doi: 10.1155/2020/8853794.

[19] N. Tervo, "Digital predistortion of millimeter-wave phased array transmitter with over-the-air calibrated simplified conductive feedback architecture," in IEEE MTT-S Int. Microw. Symp. Dig., Aug. 2020, pp. 543–546.

[20] O. Kursu, M. E. Leinonen, G. Destino, N. Tervo, M. Sonkki, T. Rahkonen, A. Pärssinen, S. Tammelin, M. Pettissalo, and A. Korvala, "Design and measurement of a 5G mmW mobile backhaul transceiver at 28 GHz," EURASIP J. Wireless Commun. Netw., vol. 2018, no. 1, p. 201, Aug. 2018.

[21] M. Jokinen, O. Kursu, N. Tervo, J. Saloranta, M. E. Leinonen, and A. Pärssinen, "Over-the-air phase measurement and calibration method for 5G mmW phased array radio transceiver," in Proc. 93rd ARFTG Microw. Meas. Conf. (ARFTG), Boston, MA, USA, Jun. 2019, pp. 1–4.

[22] N. Tyler, B. Allen, and H. Aghvami, "Adaptive antennas: The calibration problem," IEEE Commun. Mag., vol. 42, no. 12, pp. 114–122, Dec. 2004.

[23] M. E. Leinonen, M. Jokinen, N. Tervo, O. Kursu, and A. Pärssinen, "System EVM characterization and coverage area estimation of 5G directive mmW links," IEEE Trans. Microw. Theory Techn., vol. 67, no. 12, pp. 5282–5295, Dec. 2019.

[24] R. J. Mailloux, Phased Array Antenna Handbook (Artech House Antennas and Propagation Library), 2nd ed. Norwood, MA, USA: Artech House, 2005.

[25] M. E. Leinonen, G. Destino, O. Kursu, M. Sonkki, and A. Pärssinen, "28 GHz wireless backhaul transceiver characterization and radio link budget," ETRI J., vol. 40, no. 1, pp. 89–100, Feb. 2018.

[26] M. Sonkki, S. Myllymäki, N. Tervo, M. E. Leinonen, M. Sobocinski, G. Destino, and A. Pärssinen, "Linearly polarized 64-element antenna array for mm-wave mobile backhaul application," in Proc. 12th Eur. Conf. Antennas Propag. (EuCAP), Apr. 2018, pp. 1–5.

[27] S. Han, C.-l. I, Z. Xu, and C. Rowell, "Large-scale antenna systems with hybrid analog and digital beamforming for millimeter wave 5G," IEEE Commun. Mag., vol. 53, no. 1, pp. 186–194, Jan. 2015.

[28] A. F. Molisch, "Hybrid beamforming for massive MIMO: A survey," IEEE Commun. Mag., vol. 55, no. 9, pp. 134–141, Sep. 2017.

[29] N. Tervo, B. Khan, J. P. Aikio, O. Kursu, M. Jokinen, M. E. Leinonen, M. Sonkki, T. Rahkonen, and A. Pärssinen, "Combined sidelobe reduction and omnidirectional linearization of phased array by using tapered power amplifier biasing and digital predistortion," *IEEE Trans. Microw. Theory Techn.*, vol. 69, no. 9, pp. 4284–4299, Sep. 2021.

[30] M. E. Leinonen, N. Tervo, M. Sonkki, and A. Pärssinen, "Quality analysis of antenna reflection coefficient in massive MIMO antenna array module," in *Proc. 15th Eur. Radar Conf. (EuRAD)*, Sep. 2018, pp. 533–536.

[31] D. Yang, L.-L. Yang, and L. Hanzo, "DFT-based beamforming weight-vector codebook design for spatially correlated channels in the unitary precoding aided multiuser downlink," in *Proc. IEEE Int. Conf. Commun.*, Cape Town, South Africa, May 2010, pp. 1–5.

[32] C. A. Balanis, *Antenna Theory: Analysis and Design*, 3rd ed. Hoboken, NJ, USA: Wiley, 2005.

[33] M. Y. Javed, N. Tervo, R. Akbar, B. Khan, M. E. Leinonen, and A. Pärssinen, "Improving analog zero-forcing null depth with N-bit vector modulators in multi-beam phased array systems," in *Proc. IEEE 93rd Veh. Technol. Conf. (VTC-Spring)*, Apr. 2021, pp. 1–5.

[34] P. Berens, "CircStat: A MATLAB toolbox for circular statistics," *J. Stat. Softw.*, vol. 31, no. 10, pp. 1–21, 2009. [Online]. Available: https://www.jstatsoft.org/v031/i10

[35] Rohde & Schwarz GmbH & Co. (2019). *Demystifying Over-the-Air (OTA) Testing-Important Antenna Parameters, Test System Setup and Calibration.* [Online]. Available: https://www.mobilewirelesstesting.com/wp-content/uploads/2019/05/Demystifying-OTA-testing_wp_5216-3789-52_v0100.pdf

MARKKU JOKINEN (Graduate Student Member, IEEE) received the M.Sc. degree in electronics from the University of Oulu, Oulu, Finland, in 2010, where he is currently pursuing the Ph.D. degree with a focus on measurement techniques on phased array systems. He is also a Research Scientist with the Centre for Wireless Communications, University of Oulu. He has also gained experience in the design and implementation of wireless system algorithms and protocols with software-defined radio platforms.

OLLI KURSU received the M.Sc. and Ph.D. degrees in electrical and electronics engineering from the University of Oulu, Finland, in 2006 and 2015, respectively. Currently, he is a Postdoctoral Researcher with the Centre for Wireless Communications, University of Oulu. His research interests include mmW, RF, analog, and mixed signal circuit design for wireless communication systems.

NUUTTI TERVO (Member, IEEE) received the B.Sc. (Tech.), M.Sc. (Tech.), and D.Sc. (Tech.) degrees (Hons.) from the University of Oulu, Oulu, Finland, in 2014, 2014, and 2022, respectively.

His doctoral dissertation research focused on the nonlinearity and linearization of millimeter-wave beamforming transceivers. Since 2022, he has been a Postdoctoral Researcher with the Centre for Wireless Communications—Radio Technologies (CWC-RT) Research Unit, University of Oulu. He has a strong background in different fields of wireless communications, including radio frequency (RF), radio channel modeling, signal processing, and system-level analysis. Around those topics, he has already authored or coauthored more than 65 international journals and conference papers and he holds several patents. In 2019, he was a recipient of the Young Scientist Award of the URSI XXXV Finnish Convention on Radio Science, Tampere, and in 2020, he has coauthored the paper that won the 50th EuMC Microwave Prize 2020, Utrecht, The Netherlands.

AARNO PÄRSSINEN (Senior Member, IEEE) received the M.Sc., Licentiate in Technology, and Doctor of Science degrees in electrical engineering from Helsinki University of Technology, Finland, in 1995, 1997, and 2000, respectively.

From 1994 to 2000, he was with the Electronic Circuit Design Laboratory, Helsinki University of Technology, working on direct conversion receivers and subsampling mixers for wireless communications. In 1996, he was a Research Visitor with the University of California at Santa Barbara. From 2000 to 2011, he was with the Nokia Research Center, Helsinki, Finland. From 2009 to 2011, he was a member of the Nokia CEO Technology Council. From 2011 to 2013, he was with Renesas Mobile Corporation, Helsinki, as a Distinguished Researcher and the RF Research Manager. From October 2013 to September 2014, he was the Associate Technical Director of Broadcom, Helsinki. Since September 2014, he has been with the Centre for Wireless Communications, University of Oulu, Oulu, Finland, where he is currently a Professor. He leads devices and circuits research area in 6G flagship program financed by Academy of Finland. He has authored or coauthored one book, two book chapters, more than 200 international journals and conference papers, and holds several patents. His research interests include wireless systems and transceiver architectures for wireless communications with a special emphasis on the RF and analog integrated circuit and system design.

Dr. Pärssinen served as a member of the Technical Program Committee for International Solid-State Circuits Conference, in 2007 and 2017, where he was the Chair of European Regional Committee, in 2012 and 2013, and the Chair of the Wireless Sub-Committee, in 2014 and 2017. He has been serving as the Solid-State Circuits Society Representative for IEEE 5G Initiative, in 2015 and 2019. He was a recipient of European Microwave Price on the Best Paper of the European Microwave Conference, in 2020. He is also one of the original contributors to bluetooth low energy extension, now called as BT LE.

MARKO E. LEINONEN (Member, IEEE) received the M.Sc., Licentiate in Technology, and Dr. (Sc.) degrees in electrical engineering from the University of Oulu, Finland, in 1996, 2002, and 2020, respectively. From 1994 to 2012, he was with Nokia Mobile Phones, Oulu, Finland, working with various positions with radio engineering and technology management. From 2006 to 2007, he was a Senior Engineering Manager in Bengaluru, India. From 2012 to 2016, he was a Master Developer with Ericsson, Oulu. Since 2017, he has been with the Centre for Wireless Communications, University of Oulu, where he is currently a Research Director and an Adjunct Professor. He holds over 40 granted international patent families concentrating on radio engineering. His research interests include wireless radio systems and quality topics in radio engineering.

• • •